AFRL-AFOSR-VA-TR-2016-0186

Supercritical Catalytic Cracking of Hydrocarbon Feeds - Insight

Robert Rioux
PENNSYLVANIA STATE UNIVERSITY

04/21/2016
Final Report

Air Force Research Laboratory
AF Office Of Scientific Research (AFOSR)/ RTA1
Arlington, Virginia 22203
Air Force Materiel Command

REPORT DOCUMENTATION PAGE

Form Approved
OMB No. 0704-0188

PLEASE DO NOT RETURN YOUR FORM TO THE ABOVE ORGANIZATION.

1. REPORT DATE *(DD-MM-YYYY)*	2. REPORT TYPE	3. DATES COVERED *(From - To)*
13-04-2016	Final Performance Report	30-09-2012 - 30-11-2015

4. TITLE AND SUBTITLE
Supercritical catalytic cracking of hydrocarbon feeds – Insight

5a. CONTRACT NUMBER

5b. GRANT NUMBER
FA9550-12-1-0446

5c. PROGRAM ELEMENT NUMBER

6. AUTHOR(S)
Rioux, Robert, M.; Roy, Sukesh

5d. PROJECT NUMBER

5e. TASK NUMBER

5f. WORK UNIT NUMBER

7. PERFORMING ORGANIZATION NAME(S) AND ADDRESS(ES)
The Pennsylvania State University
Office of Sponsored Programs
110 Technology Center Building
University Park, PA 16802

8. PERFORMING ORGANIZATION REPORT NUMBER

9. SPONSORING/MONITORING AGENCY NAME(S) AND ADDRESS(ES)
Air Force Office of Scientific Research
875 North Randolph Street
Suite 325, Room 3112
Arlington, Virginia 22203

10. SPONSOR/MONITOR'S ACRONYM(S)

11. SPONSOR/MONITOR'S REPORT NUMBER(S)

12. DISTRIBUTION/AVAILABILITY STATEMENT
Approved for Public Release; Distribution is Unlimited

13. SUPPLEMENTARY NOTES

14. ABSTRACT
The Pennsylvania State University teamed with Spectral Energies, LLC to develop appropriate spatiotemporal imaging capabilities in single body zeolites to describe beneficial and parasitic catalytic cracking pathways. Synthetic methods to produce mordenite framework inverted (MFI) crystals with dimensions as large as 150 micron x 50 micron x 20 micron were utilized to produce catalysts that could be imaged by a suite of optical techniques, including coherent anti-Stokes Raman spectroscopy (CARS), resonance Raman spectroscopy and two-photon fluorescence. The crystals with varying Si/Al ratio were characterized by temperature programmed desorption of base probe molecules and the Al distribution in the crystals was mapped by electron probe microanalysis (EMPA). We demonstrated the ability to follow in a spatiotemporal fashion, the decomposition of the structure-directing agent used to template the zeolite during growth, and the conversion of surrogate fuels in MFI and the ability to selectively identify individual species through their vibrational/scattering fingerprints. The Penn. State group have utilized a calorimetric-based method to directly measure the heat flow during the catalytic cracking of surrogate fuels (butane, hexane and dodecane) over M

15. SUBJECT TERMS

16. SECURITY CLASSIFICATION OF:			17. LIMITATION OF ABSTRACT	18. NUMBER OF PAGES	19a. NAME OF RESPONSIBLE PERSON
a. REPORT	b. ABSTRACT	c. THIS PAGE			Robert M. Rioux
U	U	U	UU	25	19b. TELEPHONE NUMBER *(Include area code)* 814-867-2503

Reset

Standard Form 298 (Rev. 8/98)
Prescribed by ANSI Std. Z39.18
Adobe Professional 7.0

INSTRUCTIONS FOR COMPLETING SF 298

1. REPORT DATE. Full publication date, including day, month, if available. Must cite at least the year and be Year 2000 compliant, e.g. 30-06-1998; xx-06-1998; xx-xx-1998.

2. REPORT TYPE. State the type of report, such as final, technical, interim, memorandum, master's thesis, progress, quarterly, research, special, group study, etc.

3. DATES COVERED. Indicate the time during which the work was performed and the report was written, e.g., Jun 1997 - Jun 1998; 1-10 Jun 1996; May - Nov 1998; Nov 1998.

4. TITLE. Enter title and subtitle with volume number and part number, if applicable. On classified documents, enter the title classification in parentheses.

5a. CONTRACT NUMBER. Enter all contract numbers as they appear in the report, e.g. F33615-86-C-5169.

5b. GRANT NUMBER. Enter all grant numbers as they appear in the report, e.g. AFOSR-82-1234.

5c. PROGRAM ELEMENT NUMBER. Enter all program element numbers as they appear in the report, e.g. 61101A.

5d. PROJECT NUMBER. Enter all project numbers as they appear in the report, e.g. 1F665702D1257; ILIR.

5e. TASK NUMBER. Enter all task numbers as they appear in the report, e.g. 05; RF0330201; T4112.

5f. WORK UNIT NUMBER. Enter all work unit numbers as they appear in the report, e.g. 001; AFAPL30480105.

6. AUTHOR(S). Enter name(s) of person(s) responsible for writing the report, performing the research, or credited with the content of the report. The form of entry is the last name, first name, middle initial, and additional qualifiers separated by commas, e.g. Smith, Richard, J, Jr.

7. PERFORMING ORGANIZATION NAME(S) AND ADDRESS(ES). Self-explanatory.

8. PERFORMING ORGANIZATION REPORT NUMBER. Enter all unique alphanumeric report numbers assigned by the performing organization, e.g. BRL-1234; AFWL-TR-85-4017-Vol-21-PT-2.

9. SPONSORING/MONITORING AGENCY NAME(S) AND ADDRESS(ES). Enter the name and address of the organization(s) financially responsible for and monitoring the work.

10. SPONSOR/MONITOR'S ACRONYM(S). Enter, if available, e.g. BRL, ARDEC, NADC.

11. SPONSOR/MONITOR'S REPORT NUMBER(S). Enter report number as assigned by the sponsoring/ monitoring agency, if available, e.g. BRL-TR-829; -215.

12. DISTRIBUTION/AVAILABILITY STATEMENT. Use agency-mandated availability statements to indicate the public availability or distribution limitations of the report. If additional limitations/ restrictions or special markings are indicated, follow agency authorization procedures, e.g. RD/FRD, PROPIN, ITAR, etc. Include copyright information.

13. SUPPLEMENTARY NOTES. Enter information not included elsewhere such as: prepared in cooperation with; translation of; report supersedes; old edition number, etc.

14. ABSTRACT. A brief (approximately 200 words) factual summary of the most significant information.

15. SUBJECT TERMS. Key words or phrases identifying major concepts in the report.

16. SECURITY CLASSIFICATION. Enter security classification in accordance with security classification regulations, e.g. U, C, S, etc. If this form contains classified information, stamp classification level on the top and bottom of this page.

17. LIMITATION OF ABSTRACT. This block must be completed to assign a distribution limitation to the abstract. Enter UU (Unclassified Unlimited) or SAR (Same as Report). An entry in this block is necessary if the abstract is to be limited.

Final Report

(FA9550-12-1-0446)

Robert M. Rioux[1,2] and Sukesh Roy[3] (PIs)

[1]Department of Chemical Engineering, The Pennsylvania State University, University Park, PA 16802-4400 USA

[2]Department of Chemistry, The Pennsylvania State University, University Park, PA 16802-4400 USA

[3]Spectral Energies, LLC Dayton, OH USA

Executive Summary

As part of the Basic Research Initiative (BRI) on endothermic fuels, the Pennsylvania State University teamed with Spectral Energies, LLC to develop appropriate spatiotemporal imaging capabilities in single body zeolites to describe beneficial and parasitic catalytic cracking pathways. Beneficial pathways were those that led to the most desired products, including ethylene and hydrogen, while parasitic pathways led to the formation of aromatic precursors and ultimately coke. Synthetic methods to produce mordenite framework inverted (MFI) crystals with dimensions as large as 150 μm × 50 μm × 20 μm were utilized to produce catalysts that could be imaged by a suite of optical techniques, including coherent anti-Stokes Raman spectroscopy (CARS), resonance Raman spectroscopy and two-photon fluorescence. The crystals with varying Si/Al ratio were characterized by temperature programmed desorption of base probe molecules (pyridine, isopropylamine, etc.) and the Al distribution in the crystals was mapped by electron probe microanalysis (EMPA). In this part of the proposed work, we demonstrated the ability to follow in a spatiotemporal fashion, the decomposition of the structure-directing agent used to template the zeolite during growth, and the conversion of surrogate fuels in MFI and the ability to selectively identify individual species through their vibrational/scattering fingerprints. The work in this area is on-going and the combined Penn. State/Spectral Energies team continues to work on the imaging of catalytic reactions in single bodies. In the second part of the project, the Penn. State group have utilized a calorimetric-based method to directly measure the heat flow during the catalytic cracking of surrogate fuels (butane, hexane and dodecane) over MFI and faujasite (FAU) zeolites. We demonstrate for the lighter hydrocarbon (n-butane), the temporal heat flow measured directly by calorimetry agrees with the enthalpy calculated by considering the heats of formation and amount formed for all products observed in the effluent by gas chromatography-mass spectrometry (GC-MS). This is conclusively evidence that all carbon in and out of the reactor has been accounted for. As the hydrocarbon incorporates more carbon, an apparent deviation is observed between the

two techniques. The calorimetric method tends to underestimate the endotherm, suggesting that it is sensitive to exothermic chemistry occurring in the packed bed that is not accounted for in the product distribution. This is most likely due to the accumulation of aromatic and coke-like products that ultimately lead to catalyst deactivation with time on stream. Overall, we find that ZSM-5 is more effective at producing alkenes than FAU most likely due to the increased Si/Al ratio in the ZSM-5 samples examined here. Additionally, we have developed a synthesis for a hierarchical zeolite with varying Si/Al ratio that contains thin, mesoporous walls may potentially influence the catalytic cracking of hydrocarbons. This material, however, suffered from low stability at the temperatures required for catalytic cracking

Project Accomplishments

Part I (Spectral Energies/PSU)

- Acquisition and assembly of an optical microscopy system. This system uses ultrafast laser excitation to enable non-linear spectroscopic techniques such as coherent anti-Stokes Raman scattering (CARS), stimulated Raman scattering (SRS) and two-photon fluorescence (TPF).
- Implementation of a high-speed optical scanning system with multi-channel detection. This configuration allows for the acquisition of multiple signals, which are registered spatially and temporally at video rates.
- Assembly of an environmentally controlled reaction cell. This reaction cell is capable of being pressurized to >5 atm and heated to temperatures >450 °C for examination of samples under relevant reacting conditions.
- Synthesis of large (150 μm × 50 μm × 20 μm) single body zeolite crystals by hydrothermal synthesis methods. MFI, AFI and FAU were synthesized. For MFI samples, the Si/Al ratio was varied to test the influence of acidity on the chemistry within the single body.
- Studies on uncalcined zeolite samples. Several different morphologies exist in the single-body regime. The MFI, AFI, and FAU single-body morphologies were examined to determine a suitable target for further study.
- Examination of uncalcined, single-body MFI samples using non-linear spectroscopic techniques to visualize the distribution of the structure-directing agent at ambient conditions.
- Studies of single-body MFI samples undergoing decomposition of the structure-directing agent (SDA) under relevant temperature conditions using multiple non-linear spectroscopic techniques.
- Surrogate fuel studies of loading and reaction in single-body MFI using both liquid and gas phase surrogates.
- Implementation of pulse-shaping techniques for enhanced chemical selectivity of CARS and SRS signals.
- High-selectivity imaging of single-body MFI using pulse-shaping techniques for increased selectivity

Part II (PSU)

- Design and build of a high-pressure flow reactor with on-line GC/MS analysis capabilities. The systems was able to operate with liquids or gases at pressures up to 50 atm and temperatures up to 1473 K. The system was fully automated allowing long term operation.
- Integration of a Setaram Sensys EVO differential scanning calorimeter (DSC) into the above mentioned reactor system for the direct measurement of heat evolution during reaction
- Characterization of a commercial series of MFI catalysts for appropriate normalization of observed catalytic activity
- Examination of the catalytic behavior of MFI for the catalytic cracking of a number of hydrocarbons for comparison with data obtained from heat flow measurements.
- Determination of the amount of parasitic heat flow (and carbon loss) due to the occurrence of secondary reactions during catalytic cracking by comparing data from the calorimeter with product distribution and standard thermodynamic calculations.
- Synthesis and characterization of hierarchical zeolite material with mesoporosity, wide range of accessible Si/Al ratio and thin walls. It was envisioned this material might be ideal for processing larger hydrocarbon molecules. The synthesis and characterization of this material was published in Small and was granted the cover.

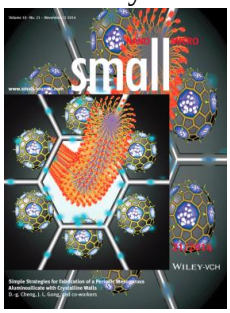

Part I. – Synopsis

Traditionally, many of the developments in the zeolite morphology and capabilities are the result of multiple iterations of development coupled with macroscale measurements of the zeolite performance. However, it is potentially the microscale structure and local activity of the zeolites that might offer the best understanding of the catalytic behavior. The understanding of the microscale structure and the associated phenomena offers a possibility for an approach to rational design of the zeolite materials. High-speed, multi-channel microscopy has been applied to study single-body reacting zeolites under reacting conditions in order to gain perspective on the microscale structure and associated phenomena. This experimental approach, based upon the use of non-linear optical spectroscopy as a contrast mechanism, provides chemically selective images with high spatial resolution. Additionally, the system has the capability to collect images at video rate and capture multiple signals simultaneously. This allows for measurements to be made *in situ*, allowing for continuous study of the same single-bodies as a function of both temperature and time spent at temperature, enabling real-time monitoring of chemical reactions with chemical selectivity and high spatial resolution.

As the system used to perform this work possesses a combination of unique capabilities, initial work focused on development and implementation of the imaging system. This included physical set-up of experimental equipment (laser, microscope, optics), as well as configuring of the electronics and scanning system to acquire multiple channels of data at high rates. Additionally, the reaction cell capabilities were characterized and necessary modifications made. Once the initial set-up was completed, effort shifted to imaging the single-body units under ambient conditions. A brief study of

zeolite morphology was performed; this was followed by studies of various chemically selective techniques. Efforts then transitioned into exploring the decomposition of the structure-directing agent. During this effort, additional studies of different aspect ratio and material activity levels were explored. Once suitable single-body formulations had been decided upon, studies to examine the loading and reaction of surrogate fuels, both liquid and gas phase, were explored. During this work, additional effort was made to use advanced pulse shaping techniques in order to enhance the chemical selectivity of the *in situ* imaging.

Part I – Instrumentation and Data Acquisition

The microscopy system was built around three central components, an ultrafast laser system, a fast optical scanning system and an upright microscope. The ultrafast laser system is an 80 MHz oscillator with dual outputs. The first output is fixed at 1040 nm with an average power of 0.750 W and a pulse duration of 220 fs. The second output is tunable from 680-1300 nm with >1.0 W of power across the entire tuning range and pulse durations of 100 fs. The tunable beam is modulated using an acousto-optic modulator (AOM) at 20 MHz. For this work, the selected wavelength is 799 nm to allow access to the C-H vibrational region at 2900 cm^{-1} for CARS and SRS. The fixed and tunable outputs are combined and directed into the fast scanning system. This system uses a resonant scanning mirror at 8 kHz to scan the fast axis and a galvanometer mirror to scan the slow axis. This scanning system is synchronized to the laser system using synchronous digitization. After passing through the scan system, the beam is sent to the upright microscope and then focused on to the sample using a 20×, 0.40 NA objective. The transmitted light is then steered away from the microscope using a silver mirror and then separated using a 750 nm dichroic. The reflected light is directed into a photo-multiplier tube (PMT) and used to collect the CARS signal after filtering out the excitation laser light. The transmitted signal passes through a wedge window, which directs a small portion of the light on to a photodiode for collection of the transmission image. The remaining transmitted light is directed onto a resonantly amplified photodiode, coupled to a lock-in-amplifier (LIA) for collection of the SRS signal.

Synchronous digitization is used to perform the data acquisition. The 80 MHz signal for the laser is used to set a master clock, which is then sent to two digitizer cards. The clock is then divided to get a 10 MHz phase-lock loop, which then feeds into the controller for the resonant mirror. In addition to triggering the resonant mirror, the controller also includes feedback analysis to maintain the phase stability of the unit. An output of 7.69 kHz from the resonant mirror controller is then inputted into an additional timing box, which controls the galvanometer mirror. The signal response from each of the detection channels is also synchronously digitized with the laser. An electronic delay on the order of 7 ns is used to maintain synchronization between the generated optical signal and the master clock signal. As the resonant mirror is driven with a sinusoidal trajectory, the collected signals must be binned in order to account for the higher sampling rates near the turning points of the mirror.

To obtain the SRS signal, lock-in-amplification was used in order to distinguish the stimulated Raman gain on the 1040 nm probe pulse. The output of the LIA is sent directly to the digitizing card. Transmission, CARS and epi-TPF signals are all sent

directly to individual channels on the digitization cards. This acquisition scheme enables 512 × 512 pixel (300 × 300 μm) images to be obtained at 15 frames per second

Part I – Results and Discussion

ZSM-5 single body crystals were synthesized by using established procedures (insert references). Crystals were grown by mixing silica sol (Ludox AS40), $Al(OH)_3$ (Sigma-Aldrich), tetrapropylammonium hydroxide (Sachem Inc. ZenGen™ SDA 746) and sodium bicarbonate (Acros Organics, 99.5%). The reacting gel of the composition $90SiO_2:Al_2O_3:12Na_2O:2100H_2O:9TPAOH$ was heated in a Teflon-lined stainless steel autoclave at 453 K, and autogeneous pressure was applied for 4 days without agitation. After completion of the process, the autoclave was quenched in cold water, the zeolite was filtered, washed with deionized water, and dried. Samples were calcined for up to 2.5 months at 550°C for removal of the TPAOH structure-directing agent.

The crystals were made with varying Si:Al ratio with a slightly modified version of the recipe above. After single body synthesis, catalysts were characterized by a number of techniques. For brevity, we only show the results electron microprobe analysis (EMPA) for determination of the Al distribution in individual crystals, and probe base molecule (pyridine, ammonia and isopropylamine) for determination of acid character and concentration. Figure 1 is an example of EMPA scans for four individual crystals. All crystals are Al-rich at the edge/rim of the crystal which decreases as the probe is rastered toward the center of the crystal. This Al zoning is well-known for large crystals formed using hydrothermal synthesis and inorganic structure-directing agents.

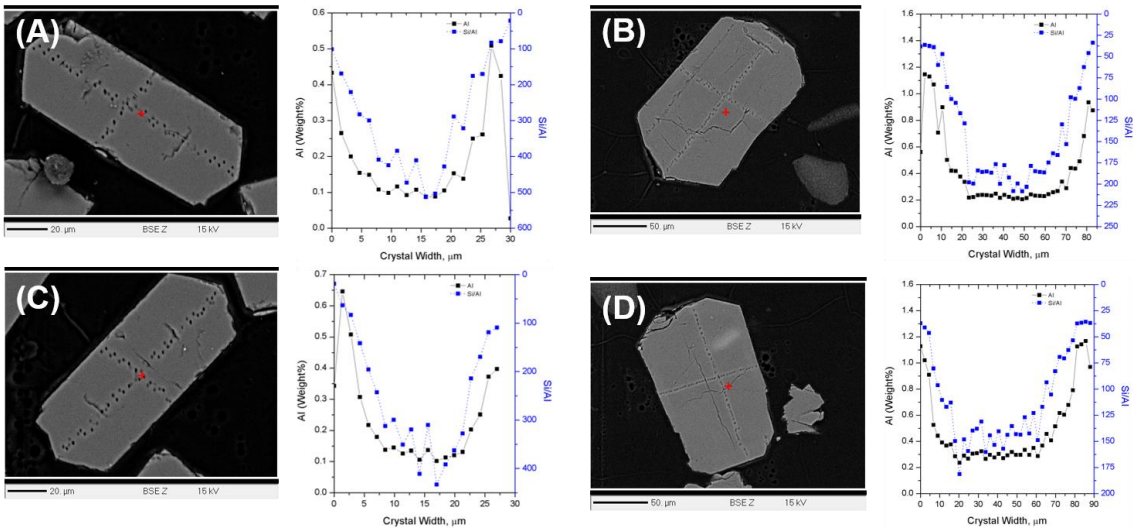

Figure 1. EMPA Al scans of single body MFI crystals with (A,C) a Si/Al ratio of 122 and (B,D) a Si/Al ratio of 48. The crystals were scanned in both the width and length dimensions but only the results of the raster scans in the width dimension are shown. The length scans demonstrate the same type of Al zoning.

The Al zoning with have implications for acid-catalyzed reactions since the highest concentration of acid sites are near to the external surface. Preliminary single body examination of propylene oligomerization demonstrates that this is indeed the case. A greater concentration of propylene and its oligmerization products were observed in the outer rim of the catalyst.

The overall acidity of catalysts was assessed by traditional base titration of Brønsted acid sites. The type of acidity (Brønsted versus Lewis) and the concentration was assessed with thermogravimetric analysis (TGA). The analyzed probe molecules included pyridine, ammonia and isopropylamine. Since isopropylamine is a commonly utilized probe molecule that decomposes to ammonia and propylene during temperature ramp when bound to Brønsted acid sites, we also interfaced a mass spectrometer to the TGA instrument. Figure 2 is an example of a typical TGA experiment utilized pyridine as a probe for acid type and concentration.

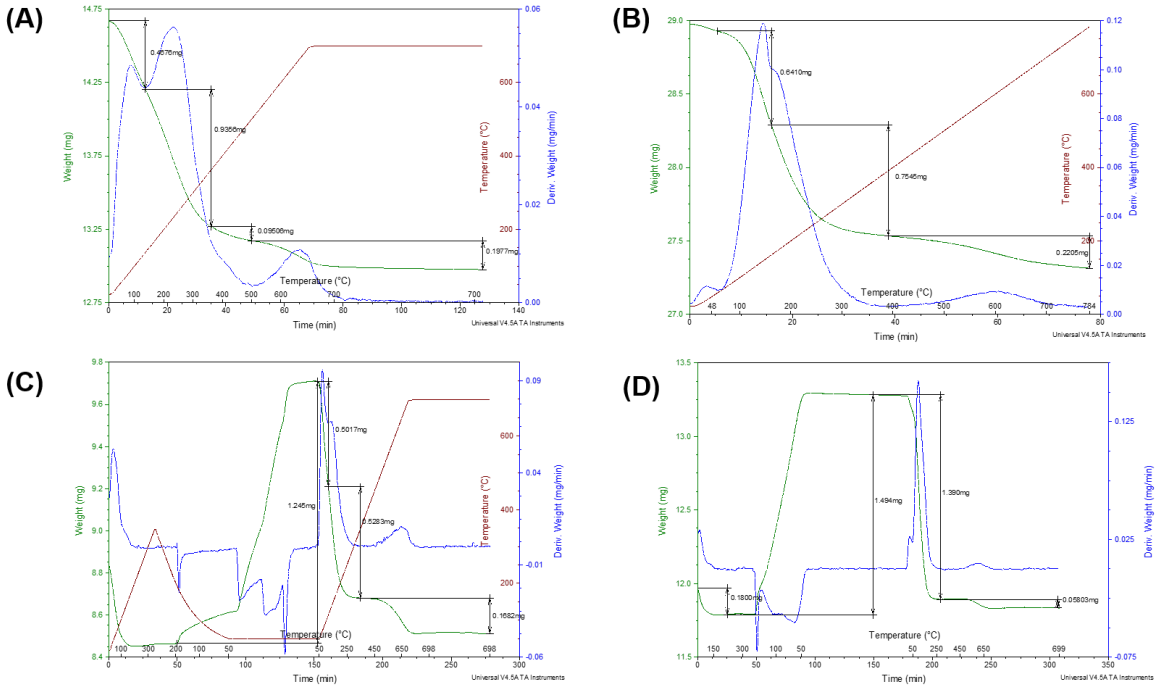

Figure 2. TGA profiles of pyridine adsorption and desorption (physisorption and chemisorption) on single body MFI crystals with a (A) Si/Al ratio of 48 and (B) a Si/Al ratio of 122. TGA profiles of pyridine adsorption and desorption (physisorption and chemisorption) on sub-micron, commercially available zeolites with a (A) Si/Al ratio of 40 and (B) a Si/Al ratio of 140. The sub-micron particle sized zeolites were obtained from Zeolyst.

The quantification of the pyridine adsorption results from TGA are summarized in Table 1. Since pyridine adsorbs to a Brønsted acid as a 1:1 adduct, the expectation is that the Si/Al should be equal to the Si/py (pyr = pyridine) if all of the Al is accessible.

Table 1. Summary of pyridine adsorption results on single body and sub-micron MFI particles with two different Si/Al ratio.

Sample Description	Si/Al ratio[a]	Si/pyr ratio[b]
CBV8014 (Zeolyst)	42 ± 1.8	41
TZ-105-3 (single body)	51 ± 1.7	57
TZ-105-3 (crushed)	51 ± 1.7	58
CBV28014 (Zeolyst)	133 ± 4.6	148
TZ-109-3 (single body)	121 ± 4.7	135
TZ-109-3 (crushed)	121 ± 4.7	136

Upon completion of the instrumentation and data acquisition system and characterization by the EMPA and temperature-programmed methods, initial single-body morphologies produced by PSU were examined. These included the FAU, MFI and AFI morphologies (Figure 3). While, the AFI morphology is not usable for catalysis, it can be used a molecular sieve, allowing diffusion of molecules of a particular size range, an aspect that may be important to developing an overall endothermic fuel system. Both the MFI and FAU morphologies are capable of use for catalytic cracking reactions. However, the geometry of the FAU results in shadowing of the images and is orientation depending, making the MFI morphology a better morphology to study. After selection of the MFI morphology, more in-depth studies began. Next, both CARS and SRS methods were applied to compare the two methodologies. Of particular interest is the ability to image the entire 3D volume of the single-body. Figure 4 shows 3D images of the SDA in single-body MFI. While both methods demonstrate the ability to clearly illuminate the entire sample volume, the CARS method suffers from background effects due to interaction and generation of the signal from the coverslip and glass slide. This non-resonant signal is a known limitation of the CARS method and serves as a reference point to avoid imaging in planes that are near the bottom surface of the single-body units. The SRS method does not suffer from the same limitation and provides uniform illumination throughout the sample volume.

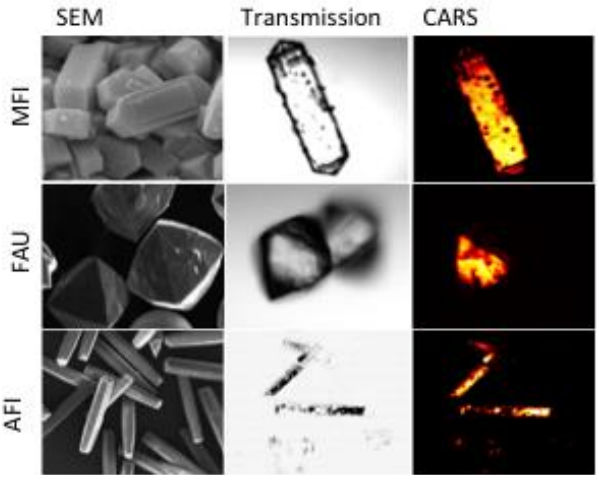

Figure 3. SEM, Optical Transmission and CARS images of the various zeolite morphologies.

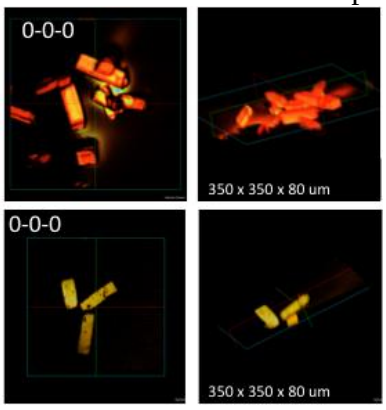

Figure 4. Volume illumination with CARS (top) and SRS (bottom) of single-body MFI structures.

Decomposition Studies

Prior to the single-bodies or any catalytic material being used for catalytic purposes, the SDA material (tri-propylamine), which fills the pores, must be removed. This process know as calcination typically occurs at temperatures in excess of 500 °C and under an oxidative environment. Understanding of the removal of the SDA material is important to the understanding of diffusion rates and porosity of the single-body units. For our studies, the samples are heated to temperatures of 350°C while exposed to atmospheric conditions. Prior to loading the samples into the reaction vessel they are dried for 48 hours to remove any water that may be adsorbed onto the sample. After loading into the reaction cell, the samples are heated at 10 °C/min while optical transmission, SRS, CARS and TPF signals are all collected simultaneously. Once the sample temperature reaches 350 °C the temperature is held constant for 30 minutes. Select images are displayed in

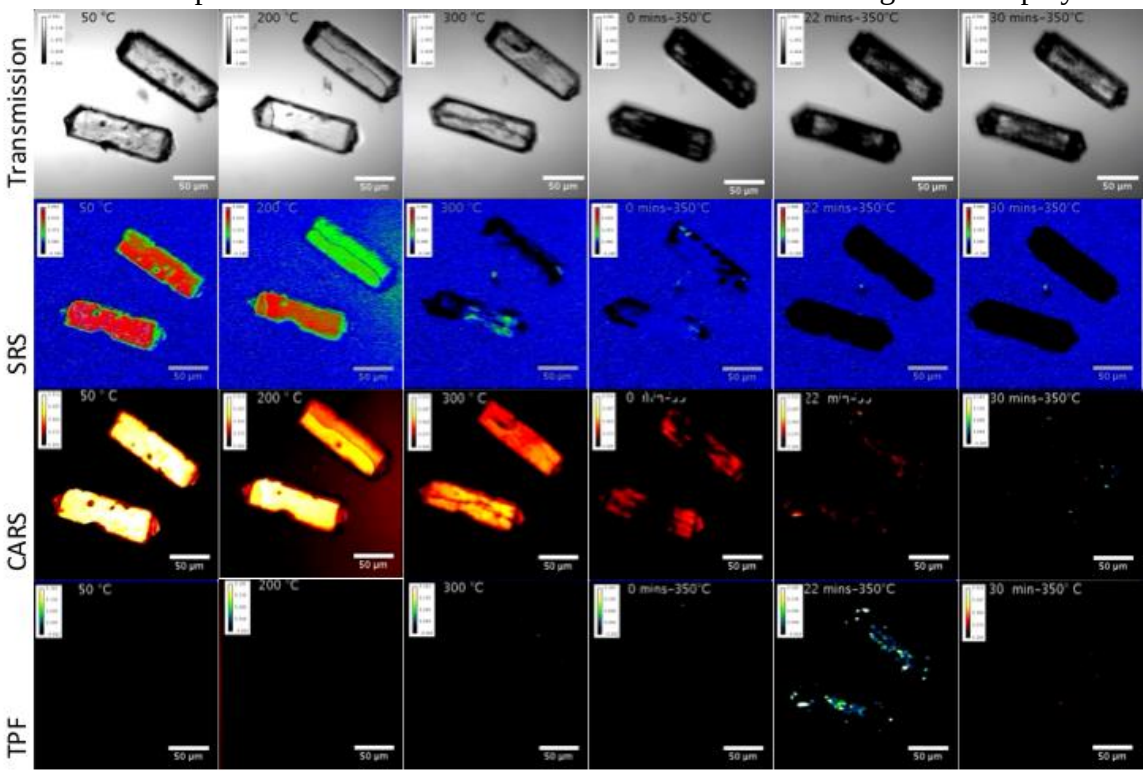

Figure 5. Transmission, SRS, CARS and TPF images simultaneously captured as single-body MFI units are heated to a temperature of 350 °C and then held for 30 minutes.

Figure 5, which illustrates observed behaviors as a function of temperature increase and time at temperature. Starting at temperatures near 300 °C, very rapid decomposition of the SDA occurs, as is evident by the darkening in the transmission image, the absorption of the incoming light in the SRS image and the decrease in signal of the CARS image. As the decomposition progresses TPF signal appears around the 10 minute mark, peaking at the 22 minute mark. The wavelength region selected for the TPF signal corresponds with that which has been previously demonstrated to correspond to the formation of large polycyclic aromatic hydrocarbons (PAHs). In fact, the observed data trends correspond very well with the hypothesized mechanism for decomposition of the SDA in which the propyl group separates from the nitrogen and is then able to undergo a series of oligomerization reactions followed by cyclization resulting in the formation of PAHs.

In addition to looking at overall trends in behavior of the system it is possible to simply look at regions of interest or how specific spatial locations behave as a function of temperature/time. For example, by selecting a small region of interest in the center of each single-body and looking at different signal responses, trends in the different signals begin to emerge. Figure 6 shows the integrated signal of the CARS and TPF responses for the same spatial location in both the top and bottom single-bodies as a function of time and temperature. For the CARS response, we see the signal begin to grow back in after ~14 mins at 350 °C after the initial decay. A similar observation can be made for the TPF signal that first appears ~14 mins at 350°C. This also corresponds to an increase in the level of light that is being able to be transmitted through the sample, suggesting that the deposits within the sample are being removed. A manuscript further detailing studies of decomposition of the SDA are in preparation.

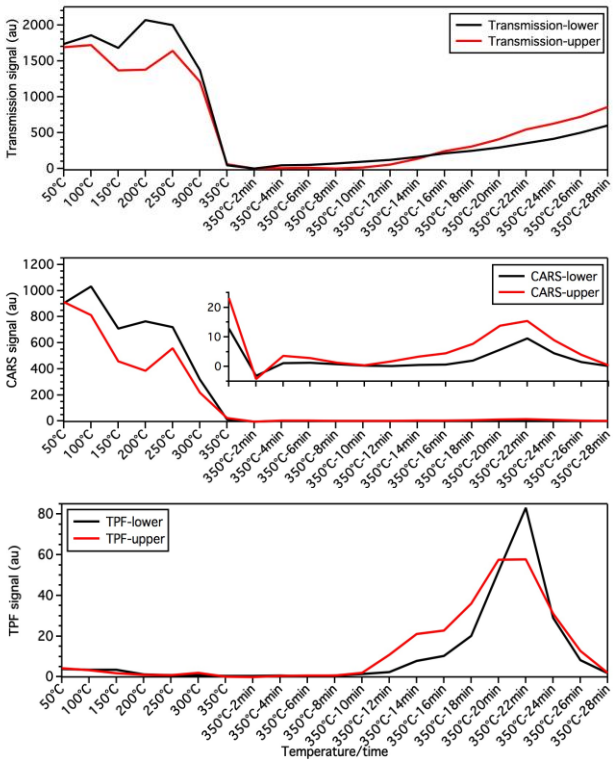

Figure 6. Integrated transmission, CARS, and TPF signals from the center region of each of the single-body units in Figure 3 as a function of temperature/time

Surrogate Fuels and Chemical Selectivity Studies

In addition to examining the decomposition of the SDA, single-component surrogate fuels were studied. Initial efforts focused on the use of liquid fuel surrogates such as hexane and dodecane. These efforts were particularly challenging with respect to getting uniform and repeatable diffusion into the pores of the single-bodies. Sample responses seemed particularly sensitive to calcination time and to the structure of the single-body themselves (Aspect ratio, silica to alumina ratio, etc.). Some samples appeared to allow diffusion of the surrogate into the pore structure, while in others the surrogate seemed to simply lay on the surface of the single-body. This effect was obvious once the samples were heated and reached the boiling point of the surrogate, as the measured CARS/SRS signal would rapidly reduce. However, in some cases, the surrogate appears to have successfully penetrated into the pore structure. In these cases, the behavior would be very similar to that observed with the decomposition of the SDA, in that the signal would decrease and conversion to coke like molecules would follow. In some cases, these reactions were very rapid, much more so than in the decomposition of the SDA material. In Figure 7, snap shots of single-body samples loaded with hexane and then heated to 400°C shows the rapid evolution of chemical changes occurring with the

single-body. These changes are only evident in the CARS and TPF signals indicating the rapid formation of large PAH type molecules.

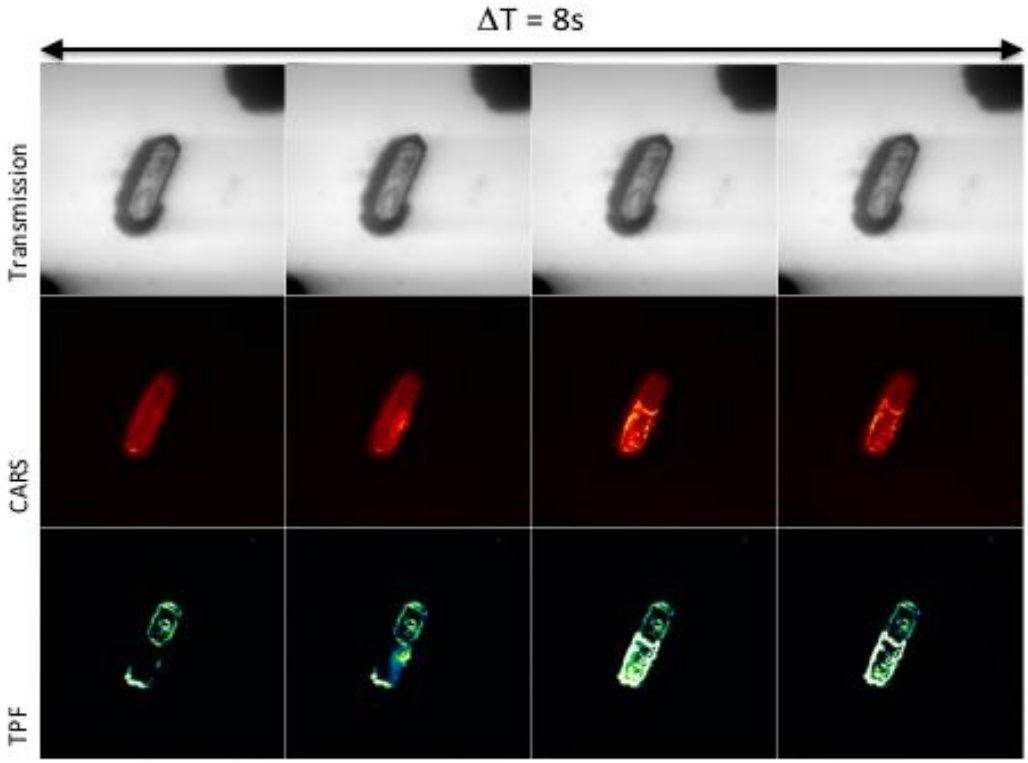

Figure 7. Transmission, CARS and TPF signal of hexane loaded single-body MFI units over an 8 second window at 400 °C where rapid evolution is evident in the CARS and TPF signals.

Attempting to simplify the use of surrogates and remove some of the unknowns associated with using liquids, the uses of gas phase species was explored. In addition to moving from liquid fuels, additional modifications were made to the optical portion of the instrument. In the previous examples, the output pulses of the laser system were used with modification only to power. As the pulses are femtosecond pulses, the frequency bandwidth of the pulses is large, ~ 130 cm^{-1} This means that all vibrational modes within the bandwidth of the pulse are excited. In the case of the C-H stretching region, which is the primary region of focus for CARS and SRS, nearly all C-H vibrational modes are excited. As an example, the aliphatic C-H vibrational mode is typically centered between 2900-2950 cm^{-1}, where as the aromatic C-H mode typically lies between 3000-3050 cm^{-1}, meaning that both modes would be excited by the broad-bandwidth pulses. However, many approaches have been demonstrated to enhance the spectral selectivity of broad-bandwidth pulses. In the

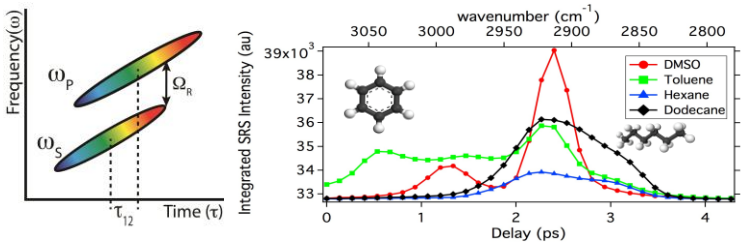

Figure 8. Schematic of spectral focusing excitation scheme and measured spectra obtained with spectral focusing of species of interest.

approach taken here, both of the excitation laser pulses pass through a highly dispersive material causing the frequency components of the pulses to stretch in time, then the relative delay between the two pulses are changed, resulting in excitation of a different frequency. Figure 8 shows an illustration of the excitation scheme as well as spectra mapped from several different species. Using this approach, peaks < 75 cm^{-1} apart are fully resolved and the C-H region can be resolved, allowing for differentiation between the aliphatic and aromatic C-H modes.

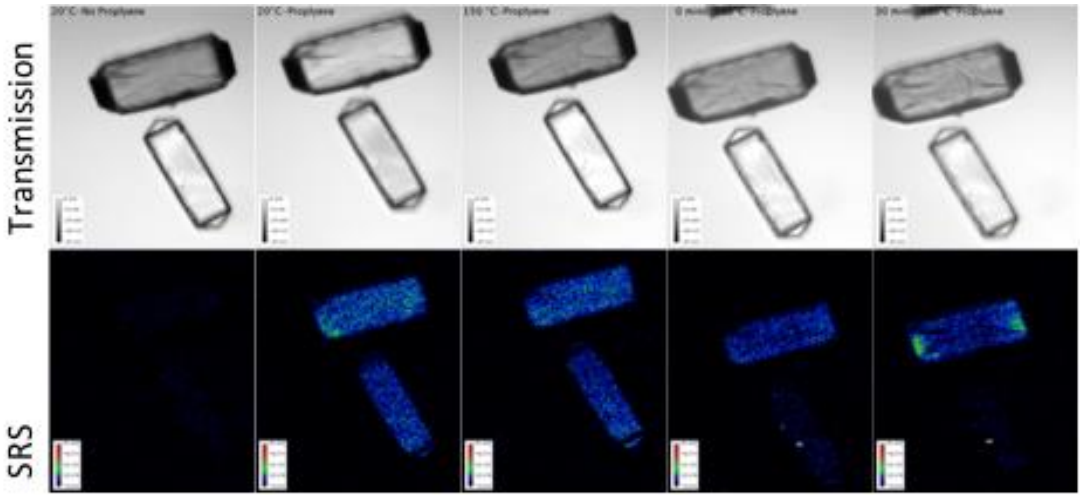

Figure 9. Transmission and SRS images of single-body MFI exposed to propylene and then heated to 300 °C.

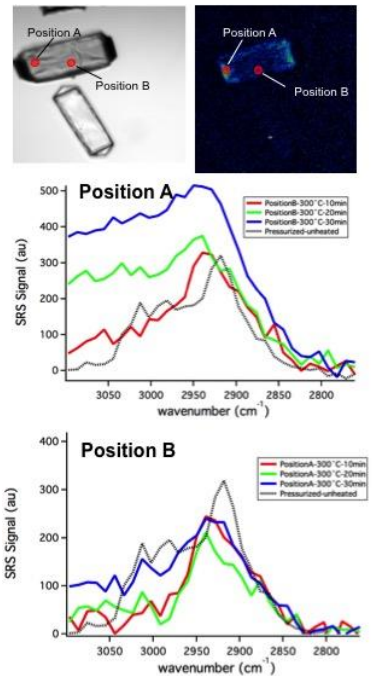

Figure 10. Transmission and SRS images at 300°C with locations marked for where spectra were generated.

This approach is very powerful in microscopy as it allows for the collection of a spectrum at every pixel in the image, or allows images to be taken at a single delay that is potentially sensitive only to a frequency of particular interest. To demonstrate this approach with the single-body MFI samples, calcined samples were exposed to gas phase propylene and pressurized to 2 atm. Once pressurized, the samples were heated to a temperature of 250 °C and then maintained for 60 mins, and then heated to 300 °C and then maintained at that temperature for 30 mins. Transmission, CARS, SRS, and TPF images were taken throughout the heating cycles, a subset of these images is shown in Figure 9. From observations of the SRS images it is apparent that different spatial locations are reacting differently as a function of temperature and time at temperature.

Using the spectral focusing technique, spectra can be assembled for various locations on the samples and at various points in the temperature/time series. Figure 10 shows spectra at different positions of the single-bodies and how the spectral signal evolves over time. In position A, the signal starts out as nearly all

aliphatic C-H signal and then transitions, containing more aromatic C-H after ~20 minutes at 300 °C. In contrast, the signal at position B, corresponding primarily to aliphatic C-H, remains nearly unchanged throughout. The use of spectral focusing for enhance chemical selectivity allows for these types of observations to be made, increasing the potential of understanding the localized chemistry *in situ*. The observations made in these studies have also inspired work to look at the distribution of active sites within the single-body. Samples loaded with propylene tend to display strong activity at the ends and edges of the single-bodies under nearly all reaction conditions and durations, implying that these are the most active areas of the unit. It has been shown that using compounds such as pyridine, it is possible to label the acid site. Current work in this area is on going.

Part II – Synopsis

As part of a larger effort to assess the ability of sub-micron zeolites (primarily MFI) to serve as an effective catalyst for catalytic cracking by producing an appropriate fuel (C_2H_4/H_2) and effective utilization of the heat sink that accompanies the endothermic cracking and dehydrogenation reactions, we examined the reactivity of MFI material with varying Si/Al ratio; ratios from ~23 to 140 were examined. The lower the ratio, the more Al incorporated into the framework. These materials are more acidic and lead to higher cracking activity, but typically reduced olefin selectivity. The reaction network of a relatively simple cracking/dehydrogenation network is shown in Scheme 1 for *n*-butane. We utilized n-butane as a probe reaction, but we also examined n-alkanes ranging from a carbon number of three (propane) up to twelve (n-dodecane). Sub-micron catalysts were characterized for their acid content by the titration of probe molecules (pyridine, isopropylamine). These results were compared with the large single body crystals.

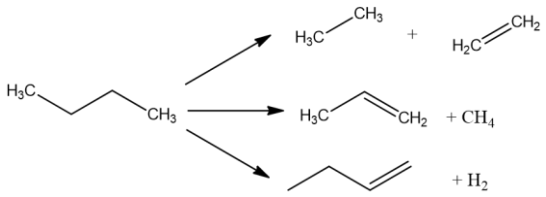

Scheme 1. Primary reactions for n-butane cracking and dehydrogenation. Products of central cracking are ethylene/ethane, while the products of terminal cracking are propylene and methane. H_2 and butane(s) are the products of the dehydrogenation pathway.

The unique aspects of the work performed by the PSU team is the direct measurement of heat flow in real time during reaction. The heat flow integrated over the duration of the reaction enabled a direct measurement of the heat of reaction, which could be compared with the product distribution determined by GC/MS and temperature-dependent heat of formation thermodynamic calculations. Comparison of the heat flow for small alkanes directly and indirectly were in close agreement with each other. As the size of the alkane increased or the temperature increased (T > 600°C), the heat flow calculated via the two methods began to diverge. We attribute this difference to occurrence of exothermic reactions that lead to product (aromatics, coke) accumulation in the catalyst bed. This led to a less endothermic heat flow measured by calorimetry. The calorimetry data also provided a better indication of when steady-state catalytic activity was achieved due to the acquisition of data points at a higher frequency.

Part II – Instrumentation and Experimental

Determination of the amount of parasitic heat flow (and carbon loss) due to the occurrence of secondary reactions during catalytic cracking by comparing data from the calorimeter with product distribution and standard thermodynamic calculations

As mentioned previously, the unique aspect of the PSU study of sub-micron zeolite particles is the integration of a differential scanning calorimeter (DSC) into the reactor set-up. This allowed for the real-time collection of heat flow data with simultaneous measurements of product concentration using GC-MS. Figure 12 is a schematic and photograph of the reactor system that was built for this project. The reactor operated in flow mode and has the capacity to flow up to four different gases. One of the gases (He) was always used for the bypass line through the reference side of the DSC. The reactor operated at temperatures up to 800°C using the DSC, or up to 1200°C if an ATS furnace was utilized. If the ATS furnace was used, there was no ability to measure heat flow. The reaction was cleanly initiated by switching from a pure He stream to one containing alkane using an electronic switching valve. The effluent from the reactor was sampled into a GC/MS.

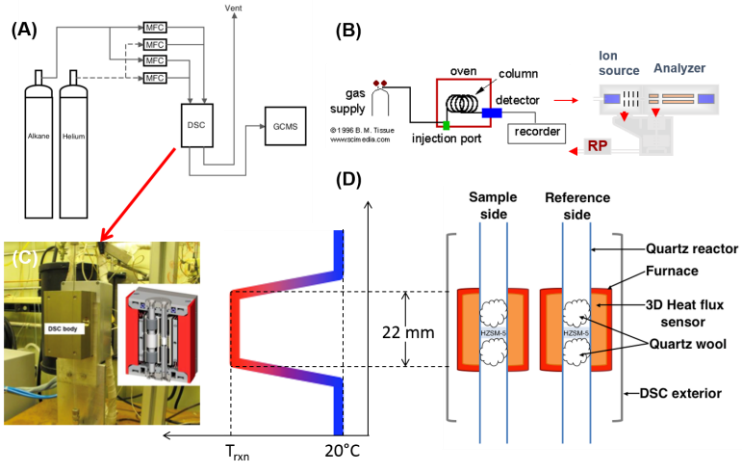

Figure 12. (A) Schematic of the high temperature and pressure reactor used for catalytic cracking reactions over sub-micron sized zeolite particles. (B) Anatomy of the GC-MS used to quantify alkane conversion and product selectivity. (C) Photograph of Setaram Sensys Evo DSC and (D) schematic of active thermopile zone in Setaram DSC.

Part II – Results and Discussion

Integration of a Setaram Sensys EVO differential scanning calorimeter (DSC) into the above mentioned reactor system for the direct measurement of heat evolution during reaction

Our primary objective of this part of the study was to measure the heat sink associated with two simple catalytic cracking reactions to ensure that the direct DSC heat flow measurement agreed with that calculated from the observed product distribution. Any deviation between these two measurements would be a direct indication of a difference in carbon balance. We started with the two simplest alkanes – propane and n-butane – that undergo primary cracking and dehydrogenation reactions. In the following section, we will examine the behavior of higher alkanes which are more relevant to endothermic cracking. Figure 13 is an example of the conversion determined by GC and the heat flow measured for *n*-butane cracking. (The reaction conditions for each is provided in the figure caption.). It is apparent that the conversion of *n*-butane is constant (X = 43 %) over the duration of the experiment which suggests that the reaction is at steady-state

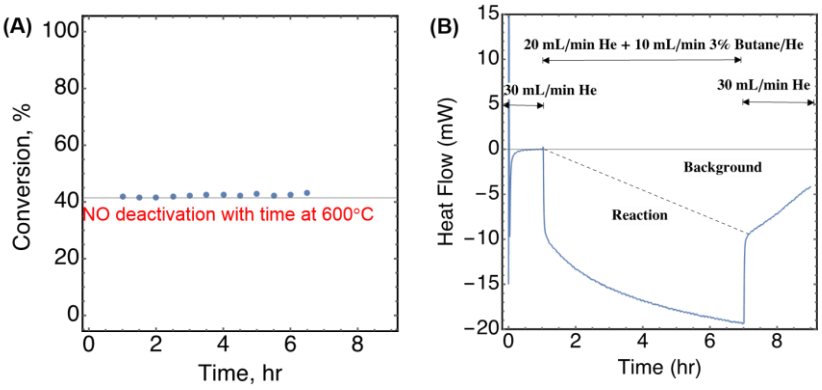

Figure 13. (A) n-butane conversion over H-ZSM-5 (Si/Al = 11.5, 25 mg) at 600°C and 1 atm. The partial pressure of butane was 10,000 ppm (1%). The conversion was constant with time-on-stream at a value of 43%. The majority of the identified products were primary products (see Figure 11) although a number of volatile secondary products were observed. (B) DSC measured heat flow as a function of time-on-stream. It is apparent that the measured heat flow has not reached steady-state even after five hours. Interestingly, this does not agree with the apparent steady-state behavior in (A). See text for further discussion.

with no apparent deactivation. However, the DSC trace does not show a steady-state behavior with regards to heat flow because it continues to become more endothermic with time-on-stream. In order to rectify this apparent inconsistency, we calculated the initial heat flow from the DSC trace (Figure 13B) and compared with the expected heat flow from the product distribution based on their heat of formation with eqn. (1).

$$(\Delta H_{rxn})_{T_f} = \left\{ \sum_{product,i=1}^{n} \frac{C_i}{C_{A,0} - C_{A,f}} \left(\Delta H_{f,i} + \int_{T_0}^{T_f} C_{p,i} \right) \right\} - \left(\Delta H_{f,A} + \int_{T_0}^{T_f} C_{p,A} \right)$$

where the first term accounts for the heat of formation of all products ($i \rightarrow n$) and the second term accounts for the heat of formation of butane. In eqn. (1), the heats of formation at 298 K are obtained from tabulated sources and corrected to the final reaction temperature (T_f) using temperature-dependent heat capacity, which is also obtained from literature sources for all observed products. The theoretical heat flow based on the conversion and product distribution is then calculated according to eqn. (2)

$$Q = F_{A,0} X \left(\Delta H_{rxn} \right)_{T_f}$$

where $F_{A,0}$ is the initial molar flow rate of *n*-butane, X is the steady-state conversion of *n*-butane and ΔH_{rxn} at T_f is the calculated heat of reaction from eqn. (1). Table 2 is a comparison of the DSC measured heat flow and that calculated from eqns. (1) and (2).

Table 2. Comparison of the heat flow and molar enthalpy for *n*-butane cracking.

Method	Heat flow (mW)	ΔH_{rxn} (kJ/mol)	ΔH_{rxn}[a] (kJ/mol)
GC-MS (indirect using eqns. 1 + 2)	11.2	113.6	90.8
DSC (direct)	11.4	115.9	

[a]Heat of reaction calculated for central cracking of n-butane.

The two methods agree nicely when the initial heat flow measured from the DSC is considered. However, as time-on-stream increases, the measured heat flow becomes more endothermic, while the product distribution and carbon balance remain unchanged (i.e., steady-state has been achieve). While the carbon balance is closed to ~ 95% each hour over the course of the experiment, the cumulative hydrocarbon pool continues to react creating a trapped product pool that continues to react. Current experiments are aimed at identifying the time evolution of the carbon species utilizing solid-state NMR and ^{13}C-labelling of the n-butane. Another indirect measure of the change in the solid catalyst was to measure the change in the temperature dependent constant pressure heat capacity (C_p) for a fresh and used catalyst. Figure 14 demonstrates that there is a significant excursion in the measured heat capacity at temperatures greater than 600°C which explains why the baseline continues to drift even though the measured *n*-butane conversion is constant. The hydrocarbon pool continues to evolve with time-on-stream that causes changes in the heat capacity of the zeolite. Since the reference side of the DSC contains fresh zeolite, the excursion of the heat flow from the initial value is attributed to reactions within the hydrocarbon pool.

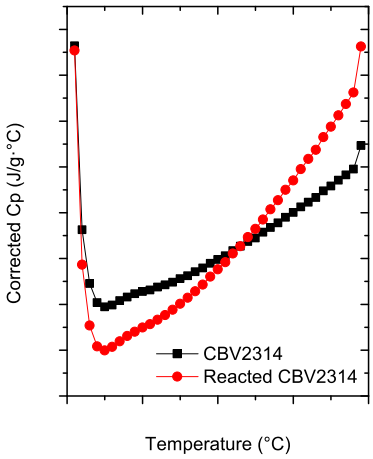

Figure 14. Temperature-dependent heat capacity measured for fresh and reacted H-ZSM5 (Si/Al =23) catalyst. At temperatures greater than 600°C, the heat capacity increases substantially for the reacted catalyst compared with used catalyst. This accounts for the increasing exotherm as a function of reaction time.

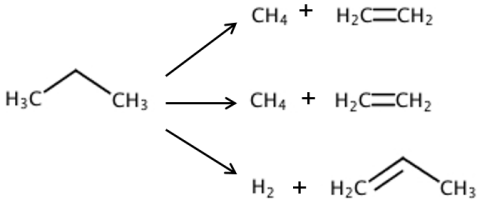

Scheme 2. Reaction network for propane cracking and dehydrogenation. The appearance of only one type of C-C bond leads to only one product (CH_4/ethylene) from cracking. Dehydrogenation of propane leads to the formation of propylene and H_2.

After observing this behavior for n-butane, we examined the reactivity and the corresponding heat flow for the cracking of simpler alkane, n-propane (Scheme 2). Since propane has only one type of C-C bond, there is only one type of cracking reaction, terminal cracking. We anticipated that the temperature excursion would be reduced due to the

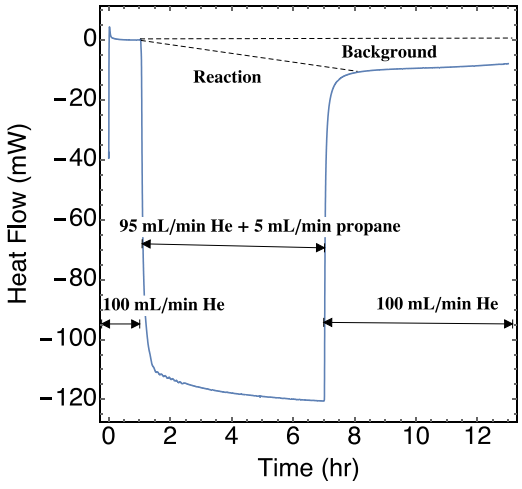

Figure 15. DSC measured heat flow as a function of time-on-stream during propane dehydrogenation. It is apparent that the measured heat flow has not reached steady-state even after five hours.

decreased number of secondary reactions even at conversions greater than those where only primary products are observed. Figure 15 is the measured heat flow for propane cracking at 600ºC over the same H-ZSM5 (Si/Al = 11.5) used for the n-butane cracking studies. One notices initially that the heat flow is significantly greater for n-propane compared to n-butane, and the baseline drift is also present during the cracking of the smaller hydrocarbon. The numerical results for the direct and indirect methods of calculation are summarized in Table 3.

Table 3. Comparison of the heat flow and molar enthalpy for *n*-propane cracking.

Method	Heat flow (mW)	ΔH_{rxn} (kJ/mol)	ΔH_{rxn}[a] (kJ/mol)
GC-MS (indirect using eqns. 1 + 2)	11.2	94.3	81.7
DSC (direct)	11.4	95.2	

[a]Heat of reaction calculated for central cracking of n-propane.

Examination of the catalytic behavior of MFI for the catalytic cracking of a number of hydrocarbons for comparison with data obtained from heat flow measurements

The data in the preceding section demonstrates the advantages of measuring the heat flow directly in real-time. It provides evidence for further reactions of the trapped hydrocarbon pool that is continually supplied with n-butane. Closure of the carbon balance up to 95% per hour still leads to significant butane hold-up and secondary reactions that we observe the influence of reactions confined to the pores of ZSM-5. We anticipate that increasing the carbon number of the hydrocarbon and therefore the complexity of the reaction network, the direct DSC measured and the indirect GC-MS-ΔH_{rxn} (T_f) method will diverge to a greater extent. For brevity, we summarize the data in Table 4. For all entries, the reaction temperature was 600°C and the conversion was maintained at ~60% by controlling the amount of catalyst. The data demonstrates that increasing the carbon number led to a significant increase in the number of products identified and the divergence between the direct and indirect method.

Table 4. Influence of carbon number on alkanes on the number of observed products and measured (direct) versus calculated (indirect) methods.

Alkane[a]	T (°C)	Conv., X (%)	Number of products quantified	Calculated enthalpy (kJ/mol)	% diff. between direct and indirect enthalpy calculation (%)
propane (3)	600	62	9	97	1.1
Butane (4)	603	59	19	121	3.1
Pentane (5)	601	65	34	128	5.2
Hexane (6)	598	54	59	135	14.2
Octane (8)	599	59	78	157	28.2
Decane (10)	600	63	97	170	31.7
Dodecane (12)	606	66	121	178	33.4

[a]Carbon number of alkane, C_nH_{2n+2} in parentheses

As the carbon number increases, the time-on-stream behavior deviates considerably from that seen with the C_3 and C_4 alkane (Figure 15). We see significant catalyst deactivation

and the excursion of the DSC signal and theoretical heat calculated by GC-MS coupled with thermodynamic calculations deviate significantly from one another. Thermogravimetric analysis of the catalysts exposed to octane, decane and dodecane showed increasing amounts of weight loss during oxidative treatment with increasing carbon number.

Synthesis and characterization of hierarchical zeolite material with mesoporosity, wide range of accessible Si/Al ratio and thin walls

In collaboration with colleagues from Tianjin University, we developed an alkali-assisted cooperative assembly process of two different templating systems with aluminosilicate precursors. With this strategy, we successfully synthesized a highly-ordered mesoporous material with mesopores of 2D hexagonal symmetry and MFI zeolitic framework walls. This versatile synthetic method allows for the preparation of ZSM-5 with *c*- or *b*-axis-aligned mesopores. The materials have acid strength and content similar to a conventional MFI zeolite with a comparable Si/Al ratio and should display promising catalytic activity for acid-catalyzed reactions involving bulky molecules. The paper was published in *Small* (**10** (2014) 4249-4256) and was granted the cover for that issue (Figure 16).

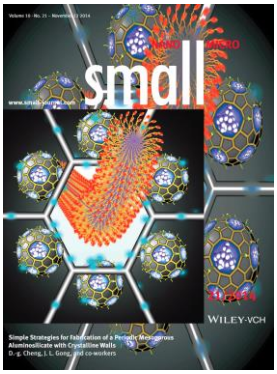

Figure 16. Rioux and Gong work profiled on the cover of Small issue (enter number).

Although assemblies of molecular and supramolecular templates have proven successful for the fabrication of both zeolites and mesoporous molecular sieves individually, the incorporation of crystalline zeolite micropores into an ordered mesopore network by cooperative assembly of two different templating systems remains a synthetic challenge because of phase separation between the mesoporous material and zeolite. This paper describes a simple and general one-step method to solve this problem using Na^+ and OH^- as promoters to enhance the cooperative assembly of an ordinary organic cation surfactant (mesotemplate) and a zeolite structure-directing agent with aluminosilicate precursors in the hydrothermal synthesis of a highly ordered periodic mesoporous aluminosilicate molecular sieve with the walls of the mesoporous composed of a crystalline zeolite framework. We denote this new, hierarchical aluminosilicate materal, PMZ-1 (Scheme 3). To illustrate our approach, we chose the cooperative assembly of tetrapropylammonium hydroxide (TPAOH) and CTAB as a model system, because they are among the most widely used SDAs for the synthesis of important ZSM-5 and MCM-41 molecular sieves, respectively. The synthetic route of the PMZ-1 was as follows. At room temperature, 5.13 g tetraethylorthosilicate, 3 g of a sol containing 3.3 wt% boehmite (obtained by hydrolysis of

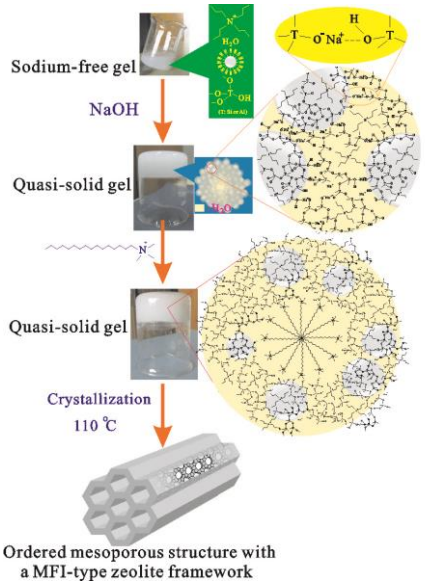

Scheme 3. Synthetic procedure for PMZ-1 and corresponding illustration of product obtained after each stage of synthesis.

aluminum isopropoxide at 85 °C for 24 h), 4 g TPAOH (25 wt% in water) was mixed with 2 g of deionized water and vigorously stirred. After stirring for 4 h, 3.5 mL of a sodium hydroxide (6 %) solution was added dropwise to obtain a quasi-solid gel containing T-O^- groups. The quasi-solid gel was combined with 1 g CTAB and further stirred for 1 h. After 10 h under static condition at room temperature, the resultant quasi-solid gel was transferred to a Teflon-coated stainless steel autoclave, and heated without stirring at 110 °C for 2 d. After crystallization, the zeolite product was washed with deionized water, then with 0.1 M HCl and repeatedly with deionized water until pH ~ 7 and dried at 60 °C for 24 h. Calcination of the products was conducted in flowing air (90 mL/min) for 5 h at 550 °C with a ramp rate of 1°C/min. A schematic of the synthesis procedure is summarized in Scheme 3. Aluminosilicate nanoparticles may be formed in a so-called clear zeolite synthesis solution obtained after hydrolysis of the silica and aluminum precursors in an aqueous TPAOH solution. Upon the addition of NaOH solution, the nanoparticles and remaining dissolved aluminosilicate species in the synthesis solution immediately condensed to form a quasi-solid gel. During formation of the quasi-solid gel, CTAB assembled into micelles. After hydrothermal crystallization at 110°C, a highly ordered mesoporous aluminosilicate with crystalline walls formed. In addition to acting as a gelation promoter, sodium hydroxide is an effective catalyst for breaking O–T (T: Si or Al) bonds in both amorphous and crystalline networks. The Na^+ and OH^--catalyzed T–O–T bond-making and bond-breaking processes can be described by the following reactions:

Scheme 4. Proposed reactions for construction of zeolite framework.

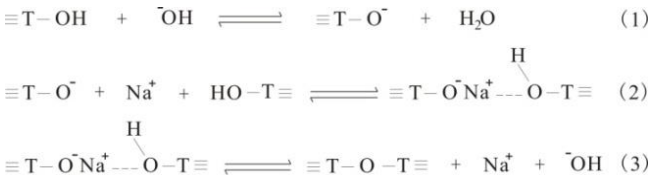

The presence of the negatively charged T–O^- groups on the surface of both the amorphous gel and the growing nuclei provides a greater driving force for electrostatic interaction of the positively charged surfactant micelles with the growing negatively charged zeolite nuclei, preventing the separate formation of mesoporous molecular sieve and zeolite.

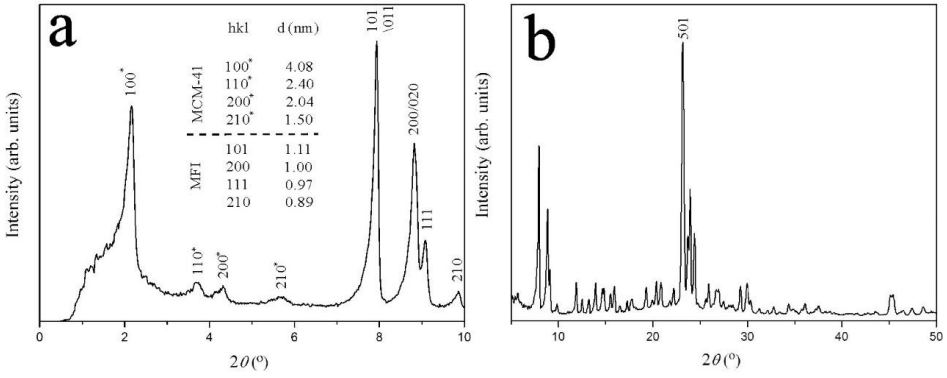

Figure 17. (a) Low- and (b) wide-angle powder XRD patterns of as-synthesized PMZ-1.

Powdered X-ray diffraction (XRD) patterns of as-synthesized PMZ-1 are shown in Figure 17. Four peaks were observed in the small-angle scattering regime ($2\theta < 6°$), with *d*-spacings of 4.08, 2.40, 2.04 and 1.50 nm, which

could be indexed to the (100), (110), (200) and (210) reflections of a 2D hexagonal symmetry (P6mm) lattice with a unit cell parameter a = 4.71 nm (a=2d_{100}/√3), similar to MCM-41. The diffractions in the rang 2θ = 6-50° can be assigned to the MFI zeolite structure. Nitrogen adsorption isotherms confirmed the existence of both uniform mesopores with diameter of 2.3 nm and 5.5 Å sized micropores, typical for 10-member ring (10-MR) channels of MFI. The mesopore size is slightly smaller than the pure mesoporous materials synthesized by a procedure similar to that for PMZ-1 except that TPAOH was used as a zeolite SDA. This could be due to densification of the mesotemplate caused by the crystallization of the walls of mesopores. The BET (Brunauer–Emmett–Teller) surface area, micropore volume and mesopore volume of the PMZ-1 were 463 m^2/g, 0.227 cm^3/g and 0.286 cm^3/g, respectively. PMZ-1 exhibited a reduction in the BET surface area and mesopore volume compared to the pure mesoporous material, once again these differences areprobably due to the crystallinity of the mesopore walls and the loss of mesopore volume by the formation of nanocrystallites within the ordered mesopores. However, the average size of ZSM-5 crystals deduced by the Debye-Scherrer's equation based on the (501) peak is about 2.40 μm. Therefore the impact of ZSM-5 nanocrystallites within the ordered mesopores could be neglected.

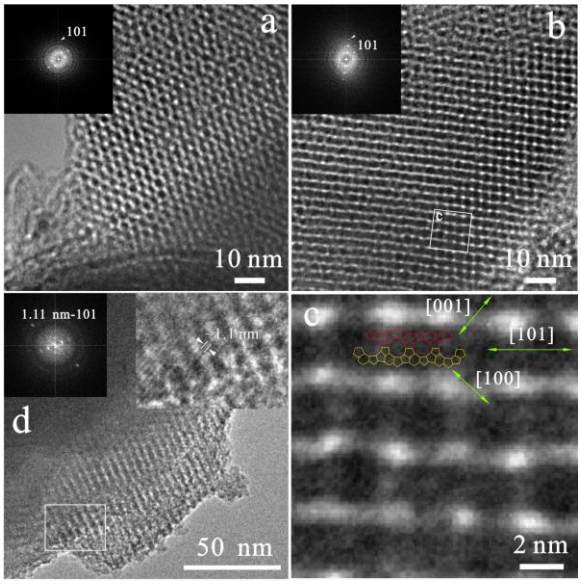

Figure 18. TEM images viewed along the (a) [001] and (b, d) [110] direction of PMZ-1 with FFTs (fast Fourier transform) as insets. The spot marked by arrowhead in the FFT of (b) correspond to a d-spacing of ~0.96 nm, which can be indexed to the $d_{[200]}$ of the MFI-type framework structure. (c) Enlarged image of the region marked by a rectangle in (b) confirms the interconnection of the MFI-type pentasil chains in the crystalline walls. The projection of the MFI framework structure with two pentasil chains growth along the [101] direction is included in (c). Top right inset of (d) is enlarged from the region outlined by the rectangle in (d) confirms the presence of ~1.1 nm spaced lattice fringes corresponding to $d_{[101]}$ of the MFI-type framework structure of the walls of the mesopores.

SEM and TEM images reveal that PMZ-1 has a globular morphology with a relatively uniform size of 0.3-2 μm with extremely small nanoparticles located on the surface of the globular particles. The nanoparticles could be due to the assembly of CTA^+ with the building units and/or zeolite nuclei formed from dissolution of defects within the crystalline domains. High-resolution transmission electron microscopy (HR-TEM) images of the PMZ-1 (Figure 18) demonstrate the pores have hexagonal symmetry with a pore center-to-center distance of 3.9-4.5 nm. The mesopore walls were composed of the MFI zeolitic framework, which contains 10-MR channels with a pore-size of 5.3 × 5.6 Å along the [010] direction, interconnected by sinusoidal 10-MR channels (5.1 × 5.5 Å) along the [100] direction. The MFI-type framework structure of the mesopore walls was confirmed not only by Fast Fourier

transform (FFT) (Figure 18a,b,d) but also by the ~1.1 nm spaced lattice fringes (i.e., pentasil chains) present in the HR-TEM images (Figure 18b-d).

The verification of the MFI zeolitic framework of the ordered mesopore walls in PMZ-1, TEM images of PMZ-1 were captured with two electron microscopes operating at low voltage (150 kV) and high voltage (300 kV). Although high-quality images of the wall structure has not yet been achieved, most likely due to the extremely thin walls and electron-beam sensitivity of the zeolite materials, it is not difficult to identify the 10-MR channels of the MFI framework. We hypothesized that increasing the crystallization temperature would lead to further growth of the zeolite framework, resulting in enhancing the thickness of the crystalline walls. To obtain further insights into the cooperative assembly of the two different templating systems (mesotemplate and zeolite structure-directing agent), we increased the crystallization temperature to 145 °C, 165 °C and 175 °C. At a crystallization temperature of 145 °C, most of the resulting mesoporous zeolite crystals had a rod-shaped structure. The mesopores run run along the *c*-axis of MFI crystal with apparent exfoliation at the ends of the nanorods (Figure S6b-g). The morphology of the product after crystallization at 145 °C are *c*-oriented nanorods and nanosheets of ZSM-5 (Figure 19). HR-TEM images (Figure 19c-d) provide direct evidence for the presence of periodic mesopores in a zeolite crystalline network. In addition to the zeolite rods with *c*-axis-aligned mesopores, an appreciable number of prism-shaped ZSM-5 crystals with *b*-axis-aligned mesopores were present in the product (Figure 19e,f). SEM and TEM images are consistent with nitrogen adsorption results showing the broadening of the mesopore size distribution with peaks centered at diameters of ~3 nm and ~5 nm. The BET surface area and mesopore volume of the 450°C-synthesized material are 356 m^2/g and 0.1 cm^3/g, respectively. These results demonstrate a significant decrease in the textural properties of the final materials with increasing synthesis temperature (110 °C to 450 °C). The periodicity of mesoporous

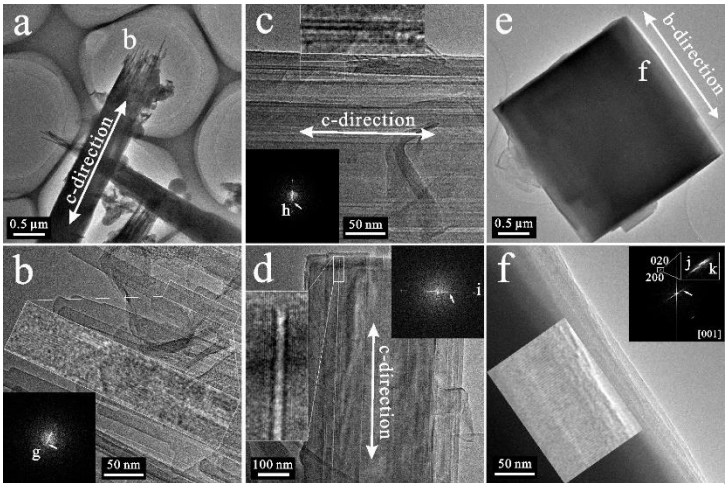

Figure 19. (a-f) TEM images of the mesoporous zeolite with different morphologies collected upon hydrothermal treatment at 450 °C for 48 h. (b-d) HR-TEM images of the rod-shaped zeolite particle in (a) demonstrate mesopores run along the *c*-direction. (e) TEM image of prism-shaped ZSM-5 crystal. (f) HR-TEM image of (e) demonstrating that the mesopores run along the *b*-direction. The FFTs contain diffuse spots due to the periodicity of the MFI microporous channels and a set of spots due to the mesoporous channel arrangement (arrows). The spots marked by g, h and i in FFT insets (b-d) correspond to a *d*-spacing ~0.92, 0.88 and 0.95 nm which can be $d_{[111]}$, $d_{[210]}$ and $d_{[200]}$ of the MFI-type framework structure. The spots marked by j and k in FFT inset (f) correspond to $d_{[200]}$ and $d_{[020]}$ of the MFI-type framework structure, respectively.

channels of the mesoporous MFI zeolites also was confirmed by the XRD reflections in the small-angle scattering regime. When the synthesis temperature is increased from 110 °C to 450 °C, the (100) and (210) reflections] of PMZ-1 gradually shift from 2θ = 2.3° and 5.6° to 3.0° and 6.5°, respectively. Simultaneously, the peaks with larger *d*-spacing values appear at about 2θ = 0.8°. This is in agreement with the large mesopore channels observed by TEM (Figure 18). The rod- and prism-shaped mesoporous ZSM-5 crystals were still obtained when the crystallization temperature was increased to 165°C. However, exfoliation of the prism-shaped mesoporous zeolite was more prominent than at 145°C, resulting in a decrease in the intensity of XRD reflections in the small-angle region. Upon further increasing the crystallization temperature to 175°C, peaks in the small-angle region characteristic of the ordered mesoporous structure gradually disappeared. SEM images display that a self-standing hierarchical zeolite monolith composed of zeolite sheets resulting from the exfoliation of the mesoporous zeolite structures formed. The formation of c-oriented sheets is confirmed by the increase in (501) peak intensity and a shift of the Bragg reflections toward higher diffraction angles. Exfoliation resulted in a decrease in the BET surface area (294 m^2/g) and the formation of disordered mesopores with a wide pore size distribution (10-50 nm) and a mesopore volume of 0.16 cm^3/g.

Acidity of porous materials is a crucial factor for their application in catalysis.

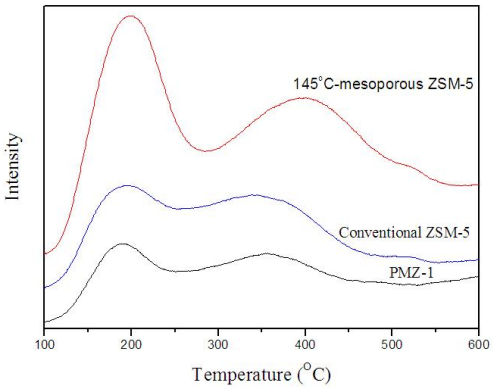

Figure 20. Ammonia TPD profiles for PMZ-1, a conventional ZSM-5, and 145°C-M-ZSM-5. The profiles confirm the presence of both strong and weak acid sites in the PMZ-1 and hierarchically mesoporous MFI zeolite obtained after hydrothermal treatment at 110°C and 145°C for 48 h, respectively. The results demonstrate that PMZ-1 has an acidity similar to the conv-MFI zeolite.

The acidity of the mesoporous materials obtained at a crystallization temperature of 110°C (PMZ-1) and 145°C (145°C -M-ZSM-5) have been investigated by temperature programmed desorption of NH_3. NH_3-TPD profiles and acid quantity (in mmol g^{-1}) of PMZ-1, Conv-ZSM-5 and 145°C-M-ZSM-5 are shown in Figure 20 and Table 5. It is apparent PMZ-1 and 145°C-M-ZSM-5 have both a low-temperature peak (~190°C) indicative of weak acid sites and a high-temperature peak (~ 360°C and ~400°C) representative of strong acid sites, which is similar to the desorption profile for a conventional-ZSM-5 zeolite. The acid quantity of PMZ-1 is smaller than the conventional-ZSM-5 zeolite. However, the acid amount in the mesoporous materials increases with increasing the crystallization temperature. PMZ-1 and 145°C -M-ZSM-5 materials contain adequate acidity and are promising materials as catalysts for reactions involving bulky organic molecules, in which the diffusion and mass transfer of reactant molecules into and out of pores is facile..

Table 5. Acid type and quantity of the samples measured by NH_3-TPD

Sample	Weak acid		Strong acid		Total Acid quantity (mmol/g)
	T (°C)	Quantity (mmol/g)	T (°C)	Quantity (mmol/g)	
PMZ-1	190	0.103	360	0.303	0.406
Conv-ZSM-5	193	0.209	352	0.548	0.757
145°C-M-ZSM-5	198	0.609	400	0.877	1.486

The characterization of the materials obtained at higher crystallization temperatures suggests lower temperature is crucial for the formation of the ordered mesoporous zeolite. Lower temperatures are most likely favorable conditions for facilitating assembly of mesotemplate to form the ordered mesopores. In addition, the amount of NaOH in the present gel system is also a critical parameter. To better understand the role of NaOH in the creation of the ordered mesoporous aluminosilicate with crystalline walls, a series of samples were synthesized with different NaOH/Si ratios at 110°C for 48 h. Material synthesized in the absence of NaOH exhibited both mesoporosity and zeolitic character (Figure 21a-d). However, SEM images (Figure 21e,f) indicate that this sample consisted of phase separated ~30 nm-sized mesoporous particles and ~1.5 μm-sized crystals of MFI zeolite, in accordance with the previous reports[43, 44]. Notably, the result confirms the addition of NaOH is necessary for the formation of the ordered mesoporous zeolite. With the addition of a relatively small amount of NaOH (NaOH/Si = 0.09), the product possesses micro- and mesoporous structures, as shown by XRD. SEM characterization indicates the product exhibits a bi-dispersed particle size population: the first consisting of ~500 nm spheres and a second consisting of 1.5 μm spherical-like particles. The larger particles appear to form due to the

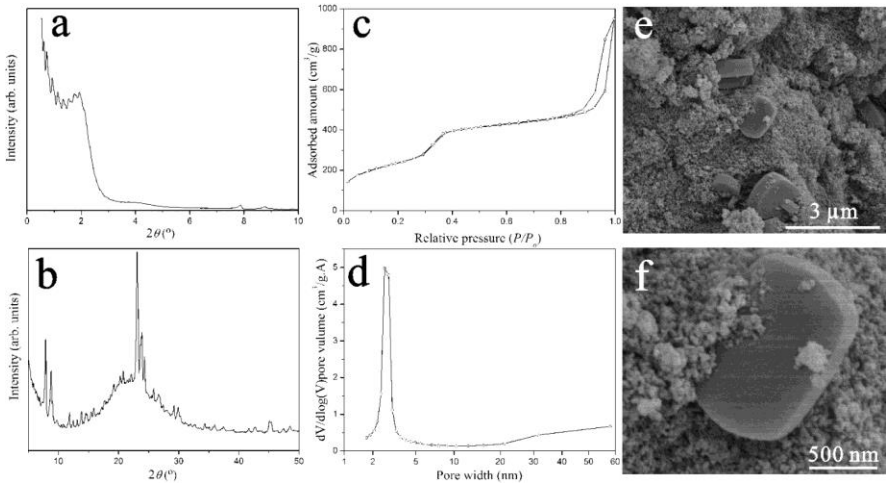

Figure 21. (a) Low- and (b) wide-angle powder XRD patterns, (c) nitrogen adsorption–desorption isotherm, (e) mesopore size distribution and (e, f) SEM images of the sample obtained after hydrothermal treatment of the gel with NaOH/Si = 0 at 110 °C for 48 h.

aggregation of the smaller size particles. Although size and morphology of the particles obtained with NaOH/Si = 0.09 are significantly different from those obtained without NaOH, the low amount of NaOH is not sufficient to inhibit the separate formation of mesoporous molecular sieve and zeolite. When the NaOH/Si ratio is increased from 0.21 (PMZ-1) to 0.27, the resultant material displays aggregates of mesoporous particles with no crystalline zeolitic phases visible from wide-angle XRD, showing an inhibiting effect of NaOH on zeolite formation.

It is noteworthy that the preparation procedure of initial gel also significantly influences the formation of the ordered mesoporous zeolite. We carried out the synthesis of a porous material similar to PMZ-1 using the procedure reported by Zhao, in which the aluminosilicate precursors were hydrolyzed in alkali solution. SEM image of the resultant material reveals large zeolite particles exist on the surface of the mesoporous particles. The phase separation may be the result of the formation of stable hydroxide precipitates of aluminum and silica during hydrolysis in alkali solution. Upon hydrolysis, the solution contained visible white particles with no apparent formation of a quasi-solid gel. This suggests the state and size of aluminosilicate species in the initial gel has substantial influence on zeolite nucleation and crystal growth.

To investigate the formation process of the ordered mesoporous zeolite, we conducted XRD and SEM studies of the samples collected at different hydrothermal treatment times at 110 °C. After hydrothermal treatment for 6 h, the resultant materials had a mesoporous structure with an amorphous framework, as proven by a broad XRD peak at about $2\theta = 2.5^{o}$ and no peak in wide angle XRD pattern. A supersaturated gel began to form on the surface of the agglomerates of mesoporous particles. This supersaturated domain appears to consist of condensed aggregates of primary sub-colloidal particles due to the dissolution of the mesoporous particles. After a reaction time of 24 h, the 20-50 nm nanoparticles aggregated on the surface of the ~2 μm sized particles. The presence of both mesoporous and MFI zeolite structures during this time is confirmed by XRD. The broad peak at 2.5^{o} indicative of the mesoporous phases decreased in intensity. This could be due to the dissolution of the mesoporous phase into solution. The surface of the mesoporous zeolite particles became relatively smooth despite still presence of the attached nanoparticles. The mesoporous zeolite particles (PMZ-1) exhibited a highly ordered mesoporous structure (four (100), (110), (200) and (210) peaks appear in the small-angle scattering regime (Figure 17a)) with a crystalline framework (Figure 18). These results suggest the mesoporous particles with amorphous walls of the mesospores convert into the mesoporous zeolite particles through a reassembly process. Further prolonging the reaction time from 48 h to 140 h, the mesostructure degraded which is confirmed by a decrease in the intensity of XRD peaks in the small-angle scattering regime. The surface of the mesoporous zeolite particles became rougher with the presence of macropores which most form due to dissolution. Simultaneously, the concentration of large coffin-shaped ZSM-5 particles increases with the apparent consumption of mesoporous zeolite particles, indicating that Ostwald ripening dominates growth at longer growth times.

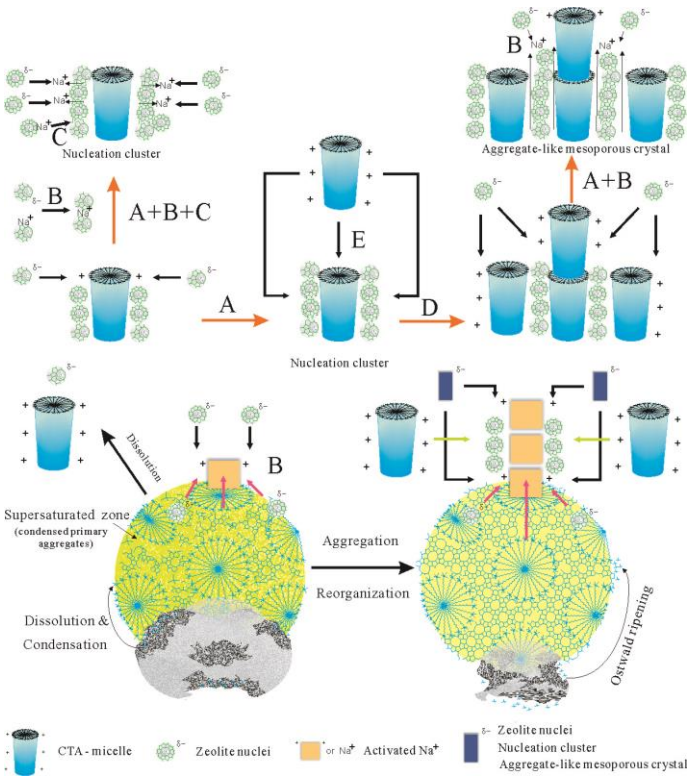

Figure 22. Schematic representation of the proposed mechanism for the formation of the mesoporous zeolite materials. Assembly at the liquid and the liquid-solid interface are driven by electrostatic forces between the positively charged surfactant micelle or active Na^+* and the negative charges of the (TO^-) groups on the surface of the aluminosilicate precursors. Assembly could occur by the following routes. The positive charge of the surfactant micelle and active Na^+* drive attachment of the nuclei by electrostatic forces (steps A, B). This attachment also leads to the formation of negatively charged aluminosilicate aggregates due to an excess of unreacted (TO^-) groups. The negative charges are continuously neutralized by assembly with active Na^+* or surfactant micelle (steps C, D). The active Na^+* participating in routes B and C can originate from released Na^+ during coalescence of near neighbor T-O-Na bond or active Na^+* present in the liquid phase.

On the basis of the above experimental observations, we propose a possible formation mechanism of the mesoporous zeolite material that involves cooperative assembly of the two different templating systems to form mesoporous zeolitic materials (Figure 22). The assembly of aluminosilicate precursors with CTA^+ micelles increases with temperature, resulting in the formation of the mesoporous particles with the walls of the mesopore being characterized as amorphous. Under hydrothermal conditions, the active Na^+* and HO^- ions are available in high concentration and quickly dissolve T–O bonds in the amorphous mesoporous particles to generate soluble $T\text{-}O^-$ and T-OH species. These soluble $T\text{-}O^-$, T-OH species are transformed into SDA-T-O species by the reaction with hydrated cations (Na^+, TPA^+, CTA^+) followed by aggregation to form primary sub-colloidal particles. The primary sub-colloidal particles further aggregate and densify into a supersaturated gel. Zeolite nucleation took place in the condensed primary aggregates by gel reorganization. The nucleation occurred at the supersaturated gel with further dissolution of the T–O bonds could lead to the movement of the nuclei into both the liquid phase and the interface of the supersaturated gel phase. In the liquid phase, nuclei assemble with CTA^+ micelle to form nucleation cluster, where these clusters continuously grow into aggregate-like mesoporous crystals via self-aggregation. The assembly is driven by electrostatic forces between the positively charged surfactant micelle or active Na^+* and the negatively charged TO^- groups on the surface of the nuclei (steps A, B). The attachments also lead to the negatively charged aluminosilicate aggregate due to

unreacted (TO^-) groups. The negative charges are continuously neutralized by assembly with the positively charged active Na^+* or surfactant micelle (steps C, D). During crystal growth in the supersaturated gel phase, the active Na^+* cations (or TPA^+, CTA^+) are expelled from the T–O–T bond network as described by reaction (3) (Na^+ ion can be substituted by TPA^+ or CTA^+). These cations most likely react preferential at the interface between the supersaturated gel and liquid phase with negatively charged nuclei (or the growing aluminosilicate precursors). In the remaining steps, self-recrystallization via coalescence and Ostwald ripening processes forms the zeolite with a system of mesopores. Increasing the crystallization temperature to 450^{o}C, the self-assembly of the surfactant micelles preferentially occurs at the extremity of the surfactant micelle (step E). Simultaneously, the aggregation between zeolite nuclei (steps B, C) dominates. The proposed scenario could lead to the formation of mesoporous zeolite rods or sheets with a decrease in mesopore density. Oriented growth also was observed in the pure mesoporous material synthesized without the zeolite SDA at 450^{o}C. At higher crystallization temperature (175°C), aggregation between zeolite nuclei which is electrostatically dominates. Coalescence of the aggregated nuclei to form T–O–T bonds of the zeolite crystal releases Na^+ and OH^-. The number of these ions increases with the growth of the zeolite crystals. At high concentrations of active Na^+ and OH^- ions, dissolution of the less stable crystalline domains or exfoliate the mesoporous structures to form zeolite sheets occurs. At the higher crystallization temperatures, decomposition of mesotemplate CTAB at high temperature may lead to exfoliation of the mesoporous zeolite crystals.

1.

1. Report Type

Final Report

Primary Contact E-mail

Contact email if there is a problem with the report.

rioux@engr.psu.edu

Primary Contact Phone Number

Contact phone number if there is a problem with the report

814-867-2503

Organization / Institution name

The Pennsylvania State University

Grant/Contract Title

The full title of the funded effort.

Supercritical catalytic cracking of hydrocarbon feeds – Insight into selectivity and stability utilizing a combined kinetic and operando non-linear spectroscopy approach

Grant/Contract Number

AFOSR assigned control number. It must begin with "FA9550" or "F49620" or "FA2386".

FA9550-12-1-0446

Principal Investigator Name

The full name of the principal investigator on the grant or contract.

Robert M Rioux

Program Manager

The AFOSR Program Manager currently assigned to the award

Chiping Li

Reporting Period Start Date

09/30/2012

Reporting Period End Date

11/30/2015

Abstract

The Pennsylvania State University teamed with Spectral Energies, LLC to develop appropriate spatiotemporal imaging capabilities in single body zeolites to describe beneficial and parasitic catalytic cracking pathways. Synthetic methods to produce mordenite framework inverted (MFI) crystals with dimensions as large as 150 ⊢ m × 50 ⊢ m × 20 ⊢ m were utilized to produce catalysts that could be imaged by a suite of optical techniques, including coherent anti-Stokes Raman spectroscopy (CARS), resonance Raman spectroscopy and two-photon fluorescence. The crystals with varying Si/Al ratio were characterized by temperature programmed desorption of base probe molecules and the Al distribution in the crystals was mapped by electron probe microanalysis (EMPA). We demonstrated the ability to follow in a spatiotemporal fashion, the decomposition of the structure-directing agent used to template the zeolite during growth, and the conversion of surrogate fuels in MFI and the ability to selectively identify individual species through their vibrational/scattering fingerprints. The Penn. State group have utilized a calorimetric-based method to directly measure the heat flow during the catalytic cracking of surrogate fuels (butane, hexane and dodecane) over MFI and faujasite (FAU) zeolites. We demonstrate for the lighter hydrocarbon (n-butane), the initial temporal heat flow measured directly by calorimetry agrees with the enthalpy calculated by considering the heats of formation and amount formed for all products observed in the effluent by mass

spectrometry, but then begins to deviate with time-on-stream. This is most likely due to the accumulation of aromatic and coke-like products that ultimately lead to changes in the catalyst but with no perturbation of time on stream (i.e., no deactivation). Additionally, we have developed a synthesis for a hierarchical zeolite with varying Si/Al ratio that contains thin, mesoporous walls may potentially influence the catalytic cracking of hydrocarbons.

Distribution Statement

This is block 12 on the SF298 form.

Distribution A - Approved for Public Release

Explanation for Distribution Statement

If this is not approved for public release, please provide a short explanation. E.g., contains proprietary information.

SF298 Form

Please attach your SF298 form. A blank SF298 can be found here. Please do not password protect or secure the PDF The maximum file size for an SF298 is 50MB.

Final Report SF298 -- RIOUX.pdf

Upload the Report Document. File must be a PDF. Please do not password protect or secure the PDF . The maximum file size for the Report Document is 50MB.

FA9550-12-1-0446 Final Report.pdf

Upload a Report Document, if any. The maximum file size for the Report Document is 50MB.

Archival Publications (published) during reporting period:

M. H. Do, T. Wang, Dang-guo Cheng, R. M. Rioux, J. Gong. Simple Strategies for Fabrication of a Periodic Mesoporous Aluminosilicate with Crystalline Walls. Small 10 (2014) 4249-4256.

A number of other publications are under various stages of preparation, revision or review.

Changes in research objectives (if any):

Not applicable

Change in AFOSR Program Manager, if any:

Not applicable

Extensions granted or milestones slipped, if any:

Not applicable

AFOSR LRIR Number

LRIR Title

Reporting Period

Laboratory Task Manager

Program Officer

Research Objectives

Technical Summary

Funding Summary by Cost Category (by FY, $K)

	Starting FY	FY+1	FY+2
Salary			
Equipment/Facilities			
Supplies			
Total			

Report Document

Report Document - Text Analysis

Report Document - Text Analysis

Appendix Documents

2. Thank You

E-mail user

Apr 15, 2016 17:30:50 Success: Email Sent to: rioux@engr.psu.edu